
ComboStoc: Combinatorial Stochasticity for Diffusion Generative Models

Rui Xu*
Shandong University
xrvitd@163.com

Jiepeng Wang*
The University of Hong Kong
jiepeng@connect.hku.hk

Hao Pan†
Microsoft Research Asia
haopan@microsoft.com

Yang Liu
Microsoft Research Asia
yangliu@microsoft.com

Xin Tong
Microsoft Research Asia
xtong@microsoft.com

Shiqing Xin
Shandong University
xinshiqing@sdu.edu.cn

Changhe Tu
Shandong University
chtu@sdu.edu.cn

Taku Komura
The University of Hong Kong
taku@cs.hku.hk

Wenping Wang
Texas A&M University
wenping@tamu.edu

Abstract

In this paper, we study an under-explored but important factor of diffusion generative models, *i.e.*, the combinatorial complexity. Data samples are generally high-dimensional, and for various structured generation tasks, there are additional attributes which are combined to associate with data samples. We show that the space spanned by the combination of dimensions and attributes is insufficiently sampled by existing training scheme of diffusion generative models, causing degraded test time performance. We present a simple fix to this problem by constructing stochastic processes that fully exploit the combinatorial structures, hence the name *ComboStoc*. Using this simple strategy, we show that network training is significantly accelerated across diverse data modalities, including images and 3D structured shapes. Moreover, *ComboStoc* enables a new way of test time generation which uses asynchronous time steps for different dimensions and attributes, thus allowing for varying degrees of control over them.

1 Introduction

Diffusion generative models rely heavily on modeling the desired behavior over the whole space of possibilities, so that the generative models cover all data distributions systematically. However, the current training schemes generally focus on a single transport path from the source pure noise distribution to the target data distribution [2, 1, 11, 10]. The training therefore gives insufficient sampling of large regions of the entire space of possibilities, which nevertheless can be stamped upon because of stochastic sampling during evaluation and produce inaccurate behavior, leading to poor generation results.

To solve this mismatch between training scheme and test time evaluation, we propose to fully sample the space of combinatorial complexity. To see why the space of possibilities has a combinatorial structure, we note that the data samples are most likely residing on high dimensional spaces with clear combinatorial structures. For example, the most powerful generative models so far use transformers

*Work done during internship at Microsoft Research Asia.

†Corresponding author.



Figure 1: *ComboStoc* improves diffusion generative models across data modalities of images and structured 3D shapes. Left: structured 3D shapes where semantic parts are colored randomly. Right: images with consistently lower Frechet Inception Distance (FID) than baseline results.

as the network model [17, 13], and treat an image sample as a collection of patch tokens to be generated in parallel; moreover, each of the patch token is encoded as a vector of high dimensions. The combination of patches and their feature vectors present highly complex spaces, over which the diffusion generative models must learn to evolve toward data samples where patches and feature vectors are correlated nontrivially. In addition, for generative tasks in more structured domains, for example, 3D shapes with semantic parts, the combinatorial complexity is even more pronounced: each part has different attributes encoding properties like its existence, bounding box and part shape, in addition to the part/patch decomposition and multiple feature channels analogous to images.

We sample the spaces of such combinatorial complexity by a simple modification of typical transport plans. In particular, instead of using a synchronized time schedule for each data sample, we apply asynchronous time steps for each of the patches/parts, attributes and feature vector dimensions, which allows for full sampling of a subspace spanning the various combinations of each pair of source and target data points.

We show that by simply enhancing the training scheme to incorporate the combinatorial sampling, the generative models for images and 3D structured shapes can be significantly improved (Fig. 1). In particular, for images from ImageNet, we obtain systematic FID-50k improvements along different training iterations than the baseline SiT model (Tab. 1). For 3D structured shapes which have even stronger combinatorial complexity, we show that our training scheme is indispensable for obtaining a working generative model.

In addition to the improved performances, the training scheme exploiting combinatorial stochasticity enables new modes of using the trained generative models. Specifically, we can now generate different patches/parts/attributes in asynchronous time schedules. This means that for example we can condition the final sample on flexible partial observations of a reference sample beyond fixed modes like binary masks. Instead, for images we can apply graded conditioning across patches and channels. For structured shapes we can also specify the shapes of some parts only, and let the model generate the rest parts and attributes. These new modes of generation have the potential to unify specialized image and shape editing solutions.

2 Background on diffusion generative models

The problem of generative modeling aims at capturing the complete distribution of a set of data samples. Its state-of-the-art solutions include denoising diffusion probabilistic models [8], score-based models [19] and flow matching [10, 11], all of which transform a simple source distribution (e.g. the unit normal distribution) into the target distribution following the dynamics specified by variations of stochastic differential equations. Remarkably, the different formulations can be unified through the framework of stochastic interpolants [2, 1]. In particular, the stochastic interpolants

Model	Params(M)	Training Steps	FID
DiT-XL	675	400K	19.5
SiT-XL	675	400K	17.2
ComboStoc	673	400K	15.69
DiT-XL	675	800K	14.3
SiT-XL	675	800K	12.6
ComboStoc	673	800K	11.41
DiT-XL (cfg=1.5)	675	7M	2.27
SiT-XL (cfg=1.5)	675	7M	2.06
ComboStoc (cfg=1.5)	673	800K	2.85

Table 1: Improvements over SiT across iterations.

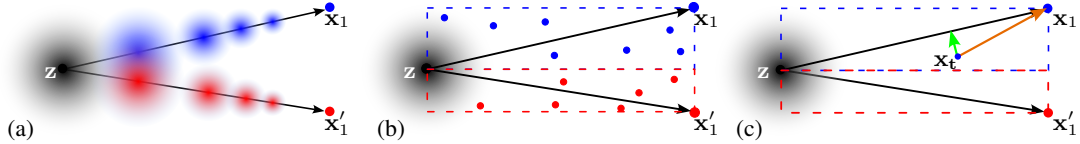


Figure 2: **ComboStoc enables better coverage of the whole path space.** Assuming two-dimensional data samples. **(a)** the standard linear one-sided interpolant model reduces its density as it approaches individual data samples; the low density regions are not well trained and once sampled would produce low-quality predictions. **(b)** using *ComboStoc*, for each pair of source and target sample points, a whole linear subspace spanned with their connection as the diagonal will be sufficiently sampled, so that there are fewer low-density regions not well trained. **(c)** when the network is trained to predict velocity $\mathbf{x}_1 - \mathbf{z}$, on an off-diagonal sample point \mathbf{x}_t , a compensation drift (\mathbf{v}_{compn} , green vector) is needed to pull the trajectory back to diagonal.

framework defines the processes of turning data samples into source distributions and vice versa as a simple interpolation between the two distributions, augmented with random perturbations during the processes. Without loss of generality, we reproduce the formulation of a simple linear one-sided interpolant process below:

$$\mathbf{x}_t = (1 - t)\mathbf{z} + t\mathbf{x}_1, t \in [0, 1] \quad (1)$$

where $\mathbf{z} \sim N(0, \mathbf{1})$ samples the source distribution, $\mathbf{x}_1 \sim D$ samples the target data distribution, $t \in [0, 1]$ is the interpolation schedule. The network model $f_\theta(\mathbf{x}_t, t)$ can be trained to recover the interpolation velocity $\frac{\partial \mathbf{x}_t}{\partial t} = \mathbf{x}_1 - \mathbf{z}$, the target data sample \mathbf{x}_1 , or the noise \mathbf{z} [1]. To generate data samples, one then starts from a random sample \mathbf{z} , follows the velocity field and integrates them numerically into the final samples.

Remarkably, on modeling large scale image datasets like ImageNet, a scalable transformer architecture implementing the above process [13] shows state-of-the-art performance and outperforms alternative formulations, including DDPM [8] implemented via the same network [17].

3 Combinatorial stochastic process

Most interesting data samples are high dimensional. For example, state-of-the-art generative models encode images as latent patches with both spatial and feature dimensions [13, 17]. 3D shapes structured as part ensembles include even more attributes in addition to spatial and feature dimensions, for example, the varying numbers of parts and their bounding boxes and positions [16]; to generate such data requires the handling of more flexible dimensions.

No matter how many dimensions and attributes a data sample has, standard diffusion generative models treat them homogeneously and in synchronization. For example, for the stochastic interpolants, the generative model is trained on samples distributed on densities with shrinking coverage along the transport paths connecting the source distribution and each target data sample, as illustrated in Fig. 2(a). The problem with this homogeneous and synchronized sampling scheme, however, is that there are low-density regions closer to the data samples that are insufficiently trained, and once they are sampled in test stage via solving stochastic differential equations, the network tends to produce poor results.

To address the above problem, we emphasize the combinatorial complexity of individual dimensions and attributes of data samples. In particular, we purposefully sample points with asynchronous diffusion schedules of dimensions and attributes, as shown in Fig. 2(b). To implement the asynchronous schedules is rather simple. We turn the interpolation schedule t of Eq. (1) into a tensor of the same shape as \mathbf{x} , and use different values within $[0, 1]$ for different dimensions or attributes:

$$\mathbf{x}_t = (1 - \mathbf{t}) \odot \mathbf{z} + \mathbf{t} \odot \mathbf{x}_1 \quad (2)$$

Correspondingly, the network $f_\theta(\mathbf{x}_t, \mathbf{t})$ is conditioned on the tensorized schedule \mathbf{t} and trained to predict velocity, or the target data sample, etc.

The benefits of using these augmented samples from combinatorial stochasticity lie in three folds:

- We make sure the network coverage is broader than the synchronized schedule, so that during test stage the network performs more robustly and with higher quality.

- We encourage the network to learn the correlations of different dimensions and attributes, as the network is trained to synchronize them to reach the final data points.
- The trained network enables more flexible conditioning, where different dimensions and attributes can be given varying degrees of finalization as specified by their interpolation schedules.

Next, we discuss the detailed adaptations and achieved effects through generative tasks from two different domains, *i.e.* images and structured 3D shapes.

Images. For image generation, we take on the baseline of SiT [13] which applies highly scalable transformer networks and achieves state-of-the-art performance on ImageNet scale generation. In particular, a given image is encoded via the VAE encoder from [18] as a latent image \mathbf{x}_1 of shape $C \times H \times W$, and the network is trained to predict velocity given the diffused latent image \mathbf{x}_t (Eq. (1)) and conditioned on the interpolation schedule t and image class c , *i.e.* $f_\theta(\mathbf{x}_t, t, c) = \mathbf{x}_1 - \mathbf{z}$.

Correspondingly, we make several simple adaptations to implement the *ComboStoc* scheme. First, we construct \mathbf{t} with the same shape of $C \times H \times W$, and update the time-step embedding module of SiT to accommodate this change (see Appendix A). Second, importantly, we note that for velocity prediction, the samples with asynchronous \mathbf{t} should not only predict the original velocity $\mathbf{x}_1 - \mathbf{z}$, but also incorporate a compensating drift that pulls the trajectory back to the diagonal path connecting the source and target points with synchronized schedules, as illustrated in Fig. 2(c). Without this off-diagonal compensation, an integration of the velocity field would lead to divergence from the target sample once any off-diagonal point is encountered. The compensation drift \mathbf{v}_{cmpn} is simply obtained as the projection of the target drift $\mathbf{x}_1 - \mathbf{x}_t$ orthogonal to diagonal, *i.e.*

$$\mathbf{v}_{cmpn}(\mathbf{t}) = \mathbf{x}_1 - \mathbf{x}_t - \frac{(\mathbf{x}_1 - \mathbf{x}_t) \cdot (\mathbf{x}_1 - \mathbf{z})}{\|\mathbf{x}_1 - \mathbf{z}\|^2} (\mathbf{x}_1 - \mathbf{z})$$

Thus the total velocity becomes $\mathbf{v}(\mathbf{t}) = \mathbf{x}_1 - \mathbf{z} + \mathbf{v}_{cmpn}(\mathbf{t})$. Note that for on-diagonal points, the compensation drift vanishes as expected.

Structured 3D shapes. We use the generative modeling of structured 3D shapes as a new task to further demonstrate the importance of exploiting combinatorial complexity. Indeed, structure 3D shapes have even stronger combinatorial complexity than images, as shown in its varying numbers of parts, their positions and bounding boxes, as well as the detailed shape variations for each part. Precisely, we denote a structured 3D object as a collection of object parts, *i.e.*, $\mathbf{x} = \{\mathbf{p}_i\}, i \in [L]$, where we set $L = 256$ to cover the maximum number of parts in a dataset. An object part is further encoded as $\mathbf{p} = (s, \mathbf{b}, \mathbf{e})$, where $s \in [0, 1]$ indicates the existence of this part, $\mathbf{b} = (x, y, z, l, w, h)$ denotes the bounding box center (x, y, z) and length l , width w and height h , and $\mathbf{e} \in \mathbb{R}^{512}$ is a latent shape code encoding the part shape in normalized coordinates. Note that under this representation, a permutation of the part indices does not change the 3D shape, which is quite different from images represented as a feature grid of fixed order and size.

To generate structured 3D shapes with semantic parts, we train a stochastic interpolant model. In particular, given a structured 3D shape $\mathbf{x}_1 = \{\mathbf{p}_i\}$ and its diffused sample \mathbf{x}_t (Eq. (2)), we make the network predict the target data sample directly for simplicity, *i.e.*, $f_\theta(\mathbf{x}_t, \mathbf{t}, c) = \mathbf{x}_1$, where c is the class condition of the 3D shape. Note that here \mathbf{t} assigns different time steps for all the different attributes and dimensions of each object part. We validate the generative model for structured 3D shapes by training on the PartNet dataset [16], as discussed in Sec. 4.

4 Results and discussion

In this part, we show that *ComboStoc* improves the training convergence of diffusion generative models for both images and structured 3D shapes. We also demonstrate the novel applications enabled by the asynchronous time steps of *ComboStoc*.

4.1 Improved training of diffusion generative models

We explore the combinatorial complexities for both images and structured 3D shapes, and build corresponding configurations which exploit these complexities to compare with baseline configurations

(a) Image domain configurations			(b) Structured 3D shape configurations		
Feature \ Spatial	w/o patch	w/ patch	Feature \ Spatial	w/o part	w/ part
single code	insync_none	insync_patch	single code	insync_none	insync_part
feature vector	insync_vec	insync_all	attribute	insync_att	insync_att_part
			feature vector	insync_vec	insync_all

Table 2: **Enumerating configurations of different combinatorial complexities**, for image domain generation (a) and structured 3D shape generation (b).

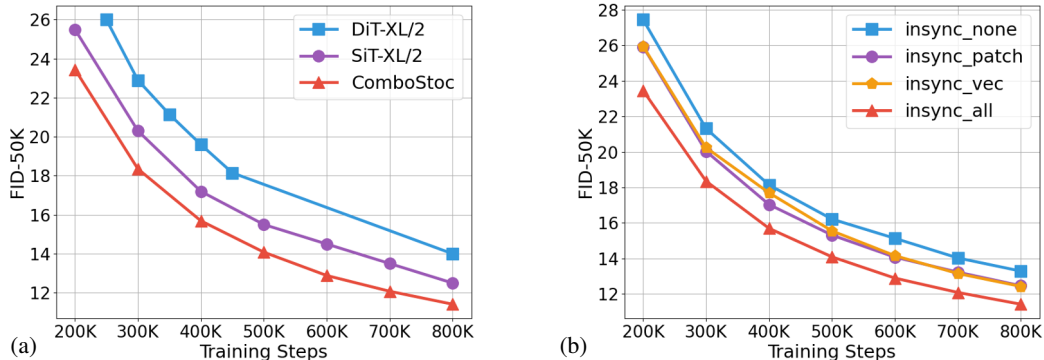


Figure 3: **Comparison on image generation with respect to training steps.** (a) plots the baseline SiT and our model, as well as DiT for reference; all models are of the scale XL/2 [13]. (b) plots the different settings using varying degrees of combinatorial stochasticity.

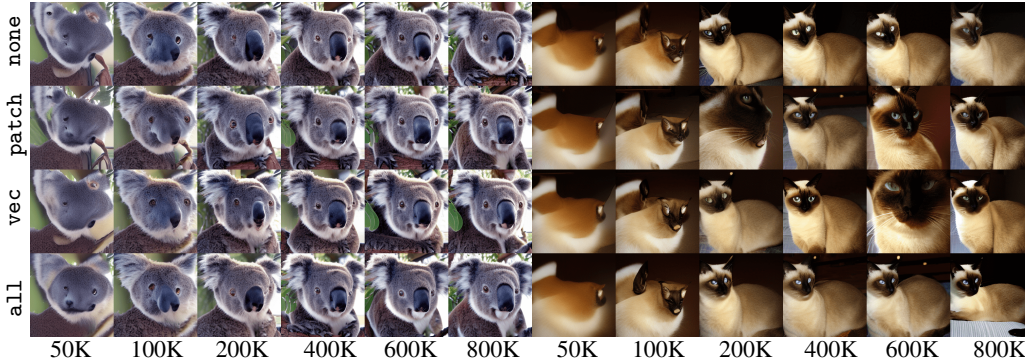


Figure 4: **Results of image generation at different training steps.** Settings with stronger combinatorial sampling produce well-structured images earlier; *e.g.* see the koala bear faces and cat eyes.

that do not apply asynchronous time schedules. We show that the different configurations improve over baseline configurations universally. In addition, we show that the higher degree of combinatorial complexity, the more important our scheme is for training a working model.

Images Following SiT [13], we train on ImageNet [3] for class-conditioned image generation. To fully explore the effects of combinatorial stochasticity, we enumerate four settings with different levels of combinatorial flexibility in diffusing the data samples (see also Tab. 2(a)). In particular, we use `insync_none`, `insync_patch`, `insync_vec`, and `insync_all` to denote no splitting of time steps, using different time steps for latent image pixels, for latent image channels, and for both image pixels and channels. We run the different settings on top of the SiT-XL/2 baseline model. Considering the difficulty posed by ImageNet data size, in each batch we apply the split time steps only to half of the samples and leave the other half unchanged with synchronized time steps, which balances between samples along and off diagonal paths (Fig. 2)³. Plots of FID-50K [7] with respect to training steps are shown in Fig. 3, where classifier-free guidance is not used.

³This batch mixing scheme may not be optimal. In preliminary tests (A) we found that blending the split time steps with synchronized ones gives even better results. The search of optimal sampling is left for future work.

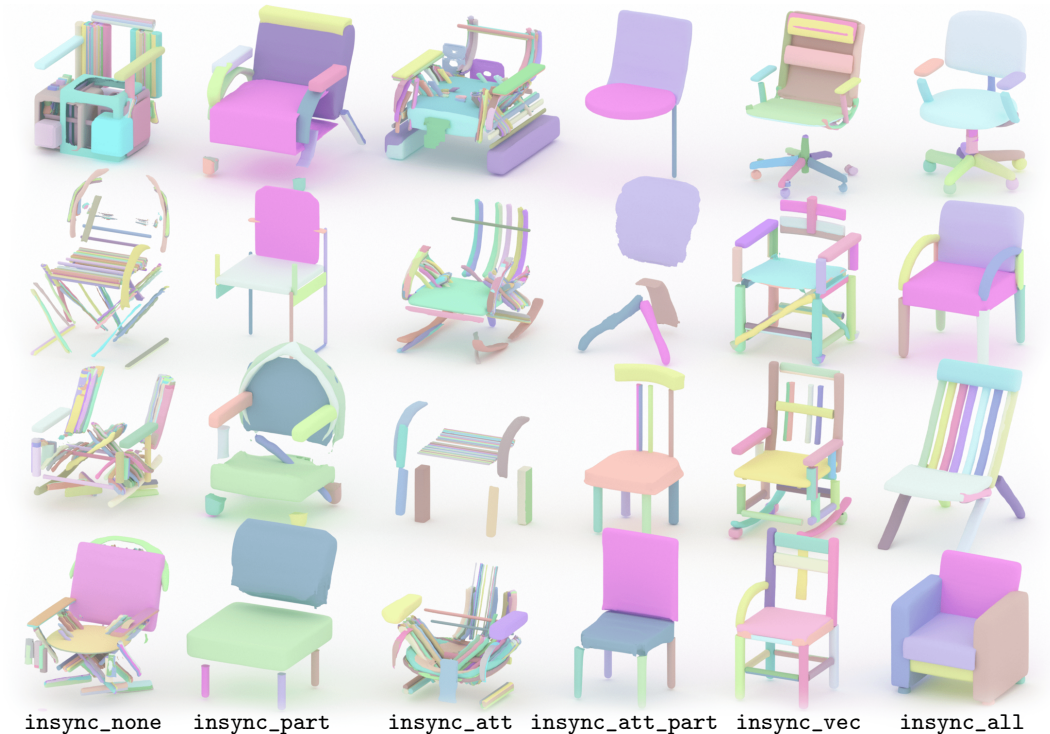


Figure 5: **Results of structured shape generation by different settings.** Semantic parts are colored randomly. Settings exploiting stronger combinatorial stochasticity show better results. In comparison, `insync_none` that does not apply *ComboStoc* nearly fails to generate meaningful shapes.

First, as shown in Fig. 3(a), our scheme (using `insync_all`) shows consistent improvement of the baseline SiT model, and significant improvement over the reference DiT model. Second, as shown in Fig. 3(b), the different settings of time step insynchronization behave differently. Overall, the finest split by `insync_all` obtains the best performances consistently, followed by `insync_vec` and `insync_patch` which split along feature and spatial dimensions and have almost indistinguishable performances. The worst performance is obtained by `insync_none`, *i.e.* the setting using no combinatorial stochasticity. Fig. 4 visualizes the results of different settings along training steps, where we see better structured images emerge earlier for settings using stronger combinatorial complexity. The comparison among these four settings shows that fully utilizing the combinatorial complexity indeed helps network training.

Note that due to the differences introduced in the time-step embedding module, `insync_none` has slightly worse performance than the baseline SiT, probably because the time-step encoding vector has a smaller size (see Appendix A). While it may be possible to align `insync_none` with baseline SiT by introducing more capable embedding layers, `insync_all` already outperforms the baseline with significant margins (Fig. 3(a)). More results by `insync_all` can be found in the Appendix A.

Structured 3D shapes We show that for the task of structured 3D shape generation, which has even stronger combinatorial complexity due to the flexible parts and their multiple attributes, our scheme becomes more important to the extent of being indispensable.

For structured 3D shape generation, we identify combinatorial complexity in the following axes: attributes/feature vectors, and spatial parts. Therefore, we obtain $3 \times 2 = 6$ settings, *i.e.*, `insync_none` and `insync_part` which apply the same or different time schedules to parts respectively, `insync_att` and `insync_att_part` which use attribute level schedules, and `insync_vec` and `insync_all` which use the most finely divided feature vector level schedules. See Tab. 2(b) for a summary of the 6 configurations. Because of the relatively small size of the PartNet dataset (18K shapes in total, mostly in *chair* and *table* classes), we deem it easier to learn and simply apply the corresponding asynchronous time steps to all samples in each batch, in contrast to the mixing scheme of ImageNet training. We report results at 1.5K epochs, since earlier results cannot be decoded into valid manifold shapes for evaluation in settings like `insync_none`.

	insync_none	insync_part	insync_att	insync_att_part	insync_vec	insync_all
FPD ↓	7.99	4.71	7.47	<u>3.51</u>	4.62	4.04
COV ↓	1.32	1.03	1.83	<u>0.85</u>	0.97	0.86
MMD ↓	1.23	1.95	1.38	1.04	<u>0.63</u>	0.68

Table 3: **Quantitative evaluation of structured shape generation by different settings.** Chair category is used. **Best** scores are marked in bold and underlined; **second best** scores in bold.



Figure 6: **Class-conditioned generation of structured 3D shapes.** From top to bottom the classes are: chair, laptop, table and display.

As shown in Fig. 5, the more combinatorial complexity we exploit, the better performance of the trained network. In comparison, the baseline setting without combinatorial stochasticity, *insync_none*, almost entirely fails to produce meaningful shapes. Moreover, since this task models the highly flexible composition of various numbers of parts, applying the spatial part insynchronization (Tab. 2(b)) helps obviously, as shown through the three pairs of columns in Fig. 5 (e.g., *part* vs *none*, *att_part* vs *att*, and *all* vs *vec*).

We report quantitative results in Tab. 3 using the chair category. Following [23] we use three metrics, including Fréchet Point Distance (FPD) that measures the FID on sampled point clouds, coverage (COV) that measures how well each GT sample is covered by the closest generated sample, and minimum matching distance (MMD) that measures how well each generated sample resembles the closest GT sample. The numerical results again show that the part level combinatorial stochasticity enhances generative performance significantly, and *insync_all* shows the best overall results.

In Fig. 6 and Appendix A we show more random samples generated by the *insync_all* setting. In Appendix A, we also compare with other works that generate structured shapes by taking a hierarchical refinement process, and find that our results are within their performance ranges.

4.2 Application enabled by combinatorial stochastic process

The asynchronous time steps for different dimensions and attributes of *ComboStoc* enables a novel test time application, namely the chance to specify different degrees of preservation of a data sample to its dimensions and attributes. Specifically, given t_0 specifying the weights in $[0, 1]$ to preserve the data of \mathbf{x} , we sample the generative process starting from

$$\mathbf{x}_0 = (1 - t_0) \odot \mathbf{z} + t_0 \odot \mathbf{x},$$

and increase the time steps for individual dimensions and attributes via $\frac{1-t_0}{N}$ for N steps. Examples of such asynchronous generative processes are shown in Figs. 7, 8 for images, and Figs. 9, 10 for structured 3D shapes.

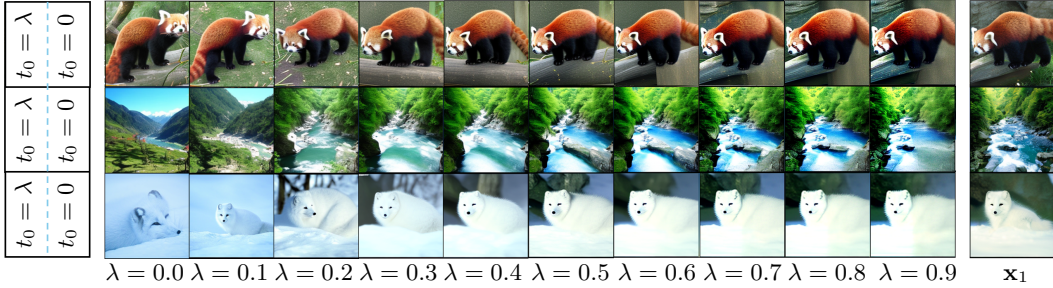


Figure 7: **Image generation using different weights of preservation.** Each reference image (right) is split into two vertical halves (left), and the left half is given the preservation weights while the right region starts from scratch.

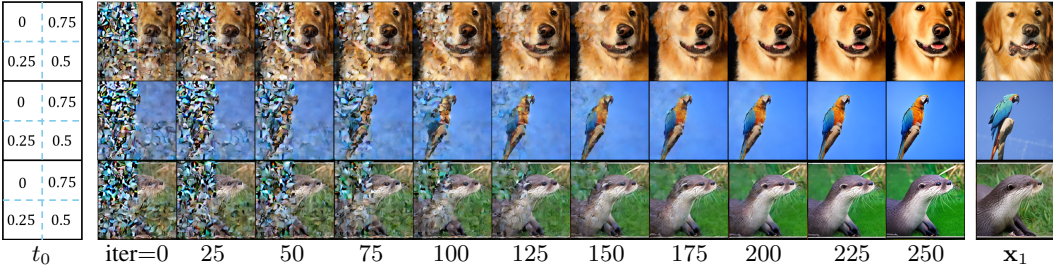


Figure 8: **Image generation with spatially different preservation weights.** As shown in the left column, the four quadrants use $t_0 = 0, 0.25, 0.5, 0.75$, respectively. The sampling iterations converge to results that preserve the corresponding quadrants from the reference images (right) differently.

Images In Fig. 7 we show that giving different t_0 to a half of a reference image while leaving the other half to generate from scratch, we can achieve different degrees of preservation of the reference images. In particular, as the preservation weight increases from 0 to 1, the preservation of reference content is strengthened. We note that at 0.5 the weight is good enough to preserve most of the reference content.

In Fig. 8, we use different preservation weights encoded by t_0 for the four quadrants of each image, and show intermediate results along the iterative SDE integration process. From the three examples we can see that stronger weights cause better preservation of reference regions, and the different regions are filled with coherent content despite the spatially varying time schedules. This mode of controlled generation is novel, compared with the binary inpainting mode proposed for standard diffusion models [12], where regions of an image are divided into two discrete types, *i.e.* those to preserve and those to generate from scratch.

Additionally in Appendix A, we show that channel-varying t_0 reveals interesting observations about the different contents of the latent image encoding [18].

Structured 3D shapes By controlling different parts and attributes of structured 3D shapes, we can achieve diverse effects, including shape completion and part assembly. In Fig. 9, we fix the bases of chairs by giving them $t_0 = 0.9$, and complete them with meaningful but diverse structures that satisfy the class condition. The given bases have the chance of being slightly updated to adapt to the completed shapes. In Fig. 10, we randomly position a set of parts, and let the network arrange them into proper shapes, by giving the part shape codes e and bounding box sizes large preservation weights ($t_0 = 0.9$) and making the rest attributes free to be generated. Here we have considered a simplified setting where the part rotations are given, and would like to explore more challenging applications where shape parts can be rotated in the future.

5 Related works

For image generation, while there are numerous optimizations of training schemes, including training loss weights and time schedules [6], speedup by distillation [14], and sampling path consistency [20], few have noticed the factor of combinatorial complexity. An exception is [5], which attributes



Figure 9: **Structured shape completion.** Given base parts (left), the network can complete the missing parts conditioned on a shape category name (`chair` in this example). While the completed parts show great diversity, the given parts are preserved faithfully.



Figure 10: **Assembly of semantic parts.** Given parts in random positions (left and right), the network assembles them into complete shapes (middle). We solve this part-assembly problem via preserving the attributes of part shapes and scales and only generating the attribute of part positions.

the slow training of DDPM based DiT model [17] to the pixel-wise regression loss, which does not emphasize the structural correlation of different patches sufficiently. To address the problem, [5] design a mask-and-diffusion scheme that masks out portions of the input diffused images during training to encourage learning the patch correlation, implemented by a complex encoder-decoder network with additional side-interpolation modules. In comparison, our scheme is simple and requires minimum changes of baseline networks, but can already improve training of SiT models significantly. Notably, SiT models already surpass DiT models in performance [13].

While 3D diffusion generative models are increasing [25, 24], few works have been done for structured shape generation. [15] studies the representation learning of hierarchically structured shapes and proposes to generate variations using a VAE model. Compared to [15], [23] proposes a rewriting model to enable generalizable cross-category generation. In comparison, we focus on generating flatly structured 3D shapes with leaf level semantic parts. Moreover, by specifying parts and attributes independently, our model enables diverse tasks like shape completion and assembly. Previously, such diverse applications have been studied individually via specialized solutions [9, 21], but here we show they can be potentially unified by a single model generating highly structured data.

6 Conclusion

We have proposed to focus on the problem of the combinatorial complexity of high-dimensional and multi-attribute data samples for diffusion-like generative models. In particular, we note that for one-sided stochastic interpolants that model many variants of diffusion and flow based models, there exists the problem of under-sampling regions of the path space where the dimensions/attributes are off-diagonal or asynchronous. We propose to fix this issue by properly sampling the whole space spanned by combinatorial complexity. Experiments across two data modalities show that indeed by fully utilizing the combinatorial complexity model, performances can be enhanced, and new generation paradigms can be enabled where different attributes of a data sample are generated in asynchronous schedules to achieve varying degrees of control simultaneously. We hope that our work can inspire future works that look through the combinatorial perspective of generative models.

Limitations and future work We did not quantify the severity of the undersampling problem for standard diffusion generative models that do not exploit the combinatorial complexity of different attributes and dimensions. Nevertheless, we conjecture that when the data samples are very densely distributed, the problem of under-sampling combinatorial complexity can be reduced. But even in that case, *ComboStoc* training still has the benefit of enabling varying degrees of conditioning in test stage applications, and encourages the learning of correlated structures among different dimensions/attributes. Practical issues like better batch time step scheduling for image generation training will also be investigated.

References

- [1] Michael S. Albergo, Nicholas M. Boffi, and Eric Vanden-Eijnden. Stochastic interpolants: A unifying framework for flows and diffusions, 2023.
- [2] Michael Samuel Albergo and Eric Vanden-Eijnden. Building normalizing flows with stochastic interpolants. In *International Conference on Learning Representations*, 2023.
- [3] Jia Deng, Wei Dong, Richard Socher, Li-Jia Li, Kai Li, and Li Fei-Fei. Imagenet: A large-scale hierarchical image database. In *Computer Vision and Pattern Recognition (CVPR)*, 2009.
- [4] Alexey Dosovitskiy, Lucas Beyer, Alexander Kolesnikov, Dirk Weissenborn, Xiaohua Zhai, Thomas Unterthiner, Mostafa Dehghani, Matthias Minderer, Georg Heigold, Sylvain Gelly, Jakob Uszkoreit, and Neil Houlsby. An image is worth 16x16 words: Transformers for image recognition at scale. *International Conference on Learning Representations*, 2021.
- [5] Shanghua Gao, Pan Zhou, Ming-Ming Cheng, and Shuicheng Yan. Masked diffusion transformer is a strong image synthesizer. In *International Conference on Computer Vision (ICCV)*, October 2023.
- [6] Tiankai Hang, Shuyang Gu, Chen Li, Jianmin Bao, Dong Chen, Han Hu, Xin Geng, and Baining Guo. Efficient diffusion training via min-snr weighting strategy. In *International Conference on Computer Vision (ICCV)*, October 2023.
- [7] Martin Heusel, Hubert Ramsauer, Thomas Unterthiner, Bernhard Nessler, and Sepp Hochreiter. Gans trained by a two time-scale update rule converge to a local nash equilibrium. In *Neural Information Processing Systems*. Curran Associates Inc., 2017.
- [8] Jonathan Ho, Ajay Jain, and Pieter Abbeel. Denoising diffusion probabilistic models. In *Neural Information Processing Systems*, volume 33. Curran Associates, Inc., 2020.
- [9] Jialei Huang, Guanqi Zhan, Qingnan Fan, Kaichun Mo, Lin Shao, Baoquan Chen, Leonidas Guibas, and Hao Dong. Generative 3d part assembly via dynamic graph learning. In *Neural Information Processing Systems (NeurIPS)*, 2020.
- [10] Yaron Lipman, Ricky T. Q. Chen, Heli Ben-Hamu, Maximilian Nickel, and Matthew Le. Flow matching for generative modeling. In *International Conference on Learning Representations*, 2023.
- [11] Xingchao Liu, Chengyue Gong, and Qiang Liu. Flow straight and fast: Learning to generate and transfer data with rectified flow. In *International Conference on Learning Representations*, 2023.
- [12] Andreas Lugmayr, Martin Danelljan, Andres Romero, Fisher Yu, Radu Timofte, and Luc Van Gool. Repaint: Inpainting using denoising diffusion probabilistic models. In *Computer Vision and Pattern Recognition (CVPR)*, June 2022.
- [13] Nanye Ma, Mark Goldstein, Michael S. Albergo, Nicholas M. Boffi, Eric Vanden-Eijnden, and Saining Xie. Sit: Exploring flow and diffusion-based generative models with scalable interpolant transformers, 2024.
- [14] Chenlin Meng, Robin Rombach, Ruiqi Gao, Diederik Kingma, Stefano Ermon, Jonathan Ho, and Tim Salimans. On distillation of guided diffusion models. In *Computer Vision and Pattern Recognition (CVPR)*, June 2023.

- [15] Kaichun Mo, Paul Guerrero, Li Yi, Hao Su, Peter Wonka, Niloy Mitra, and Leonidas Guibas. StructureNet: Hierarchical graph networks for 3d shape generation. *ACM Trans. Graph.*, 38(6), 2019.
- [16] Kaichun Mo, Shilin Zhu, Angel X. Chang, Li Yi, Subarna Tripathi, Leonidas J. Guibas, and Hao Su. PartNet: A large-scale benchmark for fine-grained and hierarchical part-level 3D object understanding. In *Computer Vision and Pattern Recognition (CVPR)*, June 2019.
- [17] William Peebles and Saining Xie. Scalable diffusion models with transformers. In *International Conference on Computer Vision (ICCV)*, October 2023.
- [18] Robin Rombach, Andreas Blattmann, Dominik Lorenz, Patrick Esser, and Björn Ommer. High-resolution image synthesis with latent diffusion models. In *Computer Vision and Pattern Recognition (CVPR)*, June 2022.
- [19] Yang Song, Jascha Sohl-Dickstein, Diederik P Kingma, Abhishek Kumar, Stefano Ermon, and Ben Poole. Score-based generative modeling through stochastic differential equations. In *International Conference on Learning Representations*, 2021.
- [20] Yang Song, Prafulla Dhariwal, Mark Chen, and Ilya Sutskever. Consistency models. In *International Conference on Machine Learning*, 2023.
- [21] Minhyuk Sung, Vladimir G. Kim, Roland Angst, and Leonidas Guibas. Data-driven structural priors for shape completion. *ACM Trans. Graph.*, 34(6), nov 2015.
- [22] Peter Walters. *An introduction to ergodic theory*, volume 79. Springer Science & Business Media, 2000.
- [23] Jiepeng Wang, Hao Pan, Yang Liu, Xin Tong, Taku Komura, and Wenping Wang. Structre: Rewriting for structured shape modeling, 2023.
- [24] Biao Zhang, Jiapeng Tang, Matthias Nießner, and Peter Wonka. 3dshape2vecset: A 3d shape representation for neural fields and generative diffusion models. *ACM Trans. Graph.*, 42(4), jul 2023.
- [25] Xin-Yang Zheng, Hao Pan, Peng-Shuai Wang, Xin Tong, Yang Liu, and Heung-Yeung Shum. Locally attentional sdf diffusion for controllable 3d shape generation. *ACM Trans. Graph.*, 42(4), jul 2023.

A Appendix

A.1 SiT adaptation for image generation

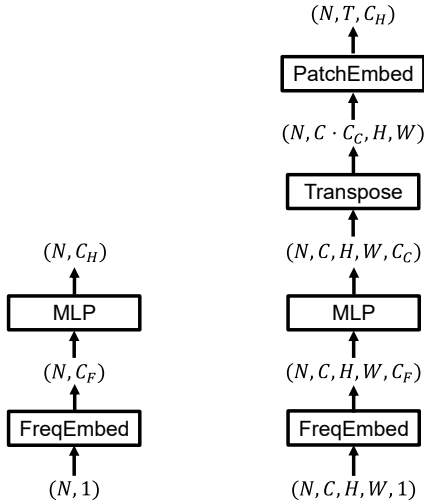


Figure 11: **Adaptation of time step embedding for ComboStoc.** **Left:** the original time step embedding module of SiT, where N is batch size, C_F is the sine/cosine frequency embedding length, and C_H is the hidden dimension of SiT transformer. **Right:** the adapted time step embedding module for ComboStoc. \mathbf{t} is now of shape (N, C, H, W) . The first two layers remain the same as the original module, applying to each entry of tensor \mathbf{t} and producing a compressed time step encoding of dim C_C . Given the result tensor of shape (N, C, H, W, C_C) , we further transpose it to combine the channel dimensions and use the same patchwise embedding layer as SiT (and ViT) to embed the local patches into vectors of dim C_H . Suppose the patch size is $L \times L$, then $T = H \times W / L^2$.

As shown in Fig. 11, given a tensorized time step \mathbf{t} of shape (N, C, H, W) that is the same as the latent encoding of input images, we not only encode each of the time steps for different dimensions as done before, but also embed the result feature map of time steps in the same way as image embedding, *i.e.* the patch-wise embedding originally from ViT [4]. This design ensures that the different dimensions are conditioned on their corresponding time steps. Note that to avoid introducing large embedding layers, we have used $C_C = 4$ to encode a time-step scalar, which is significantly smaller than the C_H of SiT. This can be the reason why `insync_none` performs slightly worse than the baseline SiT (Sec. 4), both of which have exactly the same network elsewhere.

A.2 Encoding for structured 3D shape generation

We have adopted the pretrained part shape encoding network from [23]. In particular, Wang et al. [23] design a point cloud VAE to encode 3D shapes into a sparse set of latent codes, and on top of the latent set, they train another transformer VAE to compress them into a single latent code. Therefore, each part shape from the PartNet dataset [16] is normalized into unit size and encoded into a single code, which allows us to represent structured 3D shapes as a collection of parts as detailed in Sec. 3.

The embedding modules for part existence and bounding box follow the same design as time step embedding. That is, we first turn each of the scalar dimensions into frequency codes using the sine/cosine embedding, and then embed them into vectors of dim 4 (*cf.* Fig. 11), before finally embedding each of the collective attributes as a whole into vectors of hidden dim 384, through respective FC layers.

A.3 Details of tensorized time steps

In Tab. 4 we give the details of time step specifications for all configurations, across images and structured 3D shapes. We rely on the broadcast semantics of numpy and pytorch to assign synchronized time steps to multiple dimensions.

(a) Image generation		(b) Structured 3D shapes	
Setting	\mathbf{t}	Setting	\mathbf{t}
insync_none	$(N, 1, 1, 1)$	insync_none	$(N, 1, 1)$
insync_patch	$(N, 1, H, W)$	insync_part	$(N, L, 1)$
insync_vec	$(N, C, 1, 1)$	insync_att	$(N, 1, [1, 1, 1])$
insync_all	(N, C, H, W)	insync_att_part	$(N, L, [1, 1, 1])$
		insync_vec	$(N, 1, V)$
		insync_all	(N, L, V)

Table 4: **Time step tensor shapes of different configurations.** **Left:** images are of shape (N, C, H, W) , where N is batch size, C is channel size, H and W are height and width, respectively. The \mathbf{t} tensors match up with the image tensors through broadcast semantics. **Right:** structured 3D shapes are of shape $(N, L, [V_s, V_b, V_e])$, where N is batch size, L is the number of shape parts, $[V_s, V_b, V_e]$ is the concatenation of three attributes, *i.e.*, $V_s = 1$ indicator of existence, $V_b = 6$ bounding box, $V_e = 512$ part shape code; we denote the three attributes collectively as V . \mathbf{t} tensors match up with the shape tensors through broadcast semantics.

A.4 Implementation details

The image generation model is modified from SiT-XL/2, *i.e.* the large model with 28 layers, 1152 hidden dimension, 2×2 patch size, and 16 attention heads. We trained the model using the default settings of SiT, with AdamW solver and fixed learning rate 10^{-4} , and batch size 256, on 4 Nvidia H100 gpus. The training takes 7.5 days for 800K iterations. Evaluating the models uses the SDE integrator with 250 steps. The use of classifier-free guidance (CFG) or not is specified at corresponding results. For comparison with baselines in terms of FID-50K, CFG is not used unless otherwise specified. In the result gallery figures, CFG is used with guidance strength 4.0.

The structured 3D shape generation model uses a network of SiT small model, *i.e.* the model has 12 layers, 384 hidden dimension, 256 tokens for parts and 6 attention heads. We trained the model using the AdamW solver with a fixed learning rate of 10^{-4} and batch size 16. We trained the model on 4 Nvidia A100 gpus, which takes 3 days for 1.5K epochs. Evaluating the models uses iterative sampling with 500 iterations; in each iteration, the predicted part existence is binarized via threshold 0.5 before being diffused back for next iteration. Class conditional sampling without CFG is always applied.

A.5 More results

Fig. 12 shows another example of image generation where we use varying degrees of data preservation across both spatial dimensions (the four quadrants) and feature channel dimensions. In particular, we assign spatial preservation weights according to the left column in the figure, and additionally assign 0.5 to the specified channel index C and 0 to other channels, as shown in the middle four columns. Interestingly, we see that the different channels of the stable-diffusion VAE latent space [18] have very different content. For $C = 0$ the first channel, the generated results mostly preserve the spatial structures of the reference images, and the color cues are largely lost. From $C = 1$ to $C = 3$, the generated results increasingly preserve the color cues of the reference images but lose more of the structures. The findings suggest that earlier channels of the VAE latent space emphasize on structures and later ones on image-level color distributions.

Fig. 13 shows an example of using a manually specified mask with graded preservation weights to achieve controlled generation of images. We have assigned a stronger weight ($t_0 = 0.75$) to the face of the red panda, and a lighter weight ($t_0 = 0.5$) to the region around, and let the model generate variations freely at the other regions. As expected, the generated images show different bodies for the same red panda face, with smooth transitions around the face regions.

Tab. 5 gives the comparison between our structured 3D shape generation model and two baselines, *i.e.*, StructRe [23] and StructureNet [15], in terms of FPD, COV and MMD. Shapes in PartNet are labeled into semantic parts that are organized into trees, *i.e.*, coarse parts can be decomposed into fine parts by following the tree. Exploiting this hierarchical data, the two baselines expand coarse

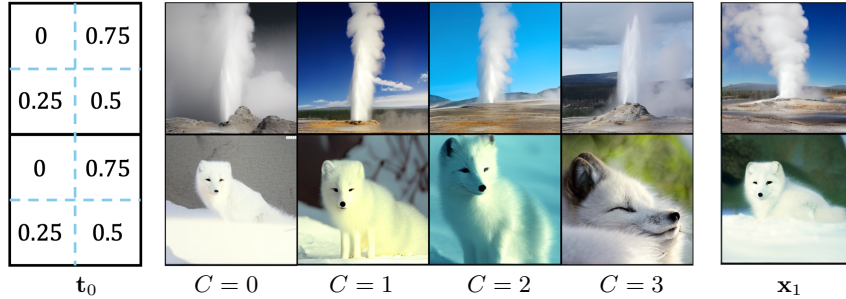


Figure 12: **Spatially and channel varying t_0** . For the spatial dimensions $t_0[:, :, i, j]$, the assignment is specified in the left column. For the feature channel dimensions $t_0[:, C, :, :]$, the C -dim is given 0.5 and the rest given 0. Therefore, we obtain results that correspond to the reference images (x_1) in complex ways. Notably, earlier channels correspond more to image structures and later channels to image colors.



Figure 13: **Customized graded t_0** . **Left** shows the t_0 map in pixels, where each pixel corresponds to a 8×8 patch of the original image. The darker region uses $t_0 = 0.75$ and the lighter region uses $t_0 = 0.5$. **Right** overlays the map over the reference image. **Middle** shows generated images.

parts into fine parts progressively, which helps constrain the generated shapes toward better regularity. In comparison, our network does not use this hierarchical information and directly generates the leaf level parts. Nevertheless, the results by `insync_all` show performances within the baseline results. Visually, we find our results generally show stronger diversity than the shapes by [23, 15]. Finally, it is an interesting topic to study how to combine the approaches of hierarchical generation and diffusion generative models, which have differing advantages in aspects of structure regularity and diversity.

Fig. 14 shows results from preliminary tests on a different scheme of batch mixing for image generative model training (Sec. 4). For training this model named *ComboStoc-TB*, we simply blend the asynchronous time steps and the synchronized ones for a whole batch. In addition, we try to align the time step embedding module with the baseline SiT by setting $C_C = C_H$ (Fig. 11). The two

Category	Method	FPD↓	COV↓	MMD↓
chair	StructureNet	4.67	0.89	<u>0.58</u>
	StructRe	<u>2.63</u>	<u>0.70</u>	<u>0.65</u>
	Ours	4.04	0.86	0.68
table	StructureNet	6.07	1.43	<u>0.55</u>
	StructRe	<u>1.98</u>	<u>0.66</u>	<u>0.53</u>
	Ours	3.43	1.20	0.72

Table 5: **Comparison on structured 3D shape generation**. Our results are comparable to the baselines that additionally use the hierarchies of shape parts to constrain generations. **Best** scores are marked in bold and underlined; **second best** scores in bold.

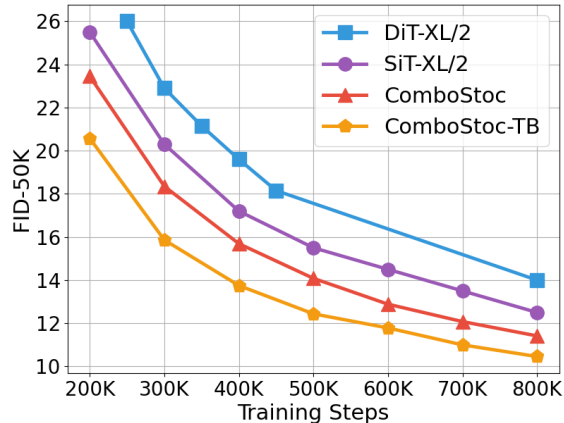


Figure 14: **A different scheme of batch mixing for training image generative model.** Plots include our **baseline model** (*ComboStoc*) and the **new batch mixing model** (*ComboStoc-TB*), as well as DiT and SiT for reference; all models are of the scale XL/2 [13].

modifications combined lead to even larger improvements over baselines. Indeed, *ComboStoc-TB* speeds up the convergence of SiT by $\approx 1.75\times$. We plan to investigate these modifications thoroughly in the future.

Figs. 15 to 30 show more results generated by *ComboStoc* models for both structured 3D shapes and images.

A.6 Broader impact

In this paper we have presented *ComboStoc* which improves and extends baseline diffusion generative models, across tasks of image generation and structured 3D shape generation. Image generation can be misused potentially, although our model as well as the baseline model uses very coarse level class name conditioning that prevents highly targeted applications. Structured 3D shapes are mostly furniture like daily objects, so their generation is unlikely to be misused. In terms of methodology, we have advocated the importance of sampling the combinatorial flexibility for both model performance and new applications. The combinatorial complexity of high-dimensional and multiple-attribute data samples can be further explored theoretically based on our work, for example from the perspective of ergodicity [22] as emphasized by our dense sampling of all possible interpolation points.



Figure 15: Class-conditioned structured 3D shapes generated by *ComboStoc*. Class label is chair.



Figure 16: Class-conditioned structured 3D shapes generated by *ComboStoc*. Class label is bed.



Figure 17: Class-conditioned structured 3D shapes generated by *ComboStoc*. Class label is `table`.

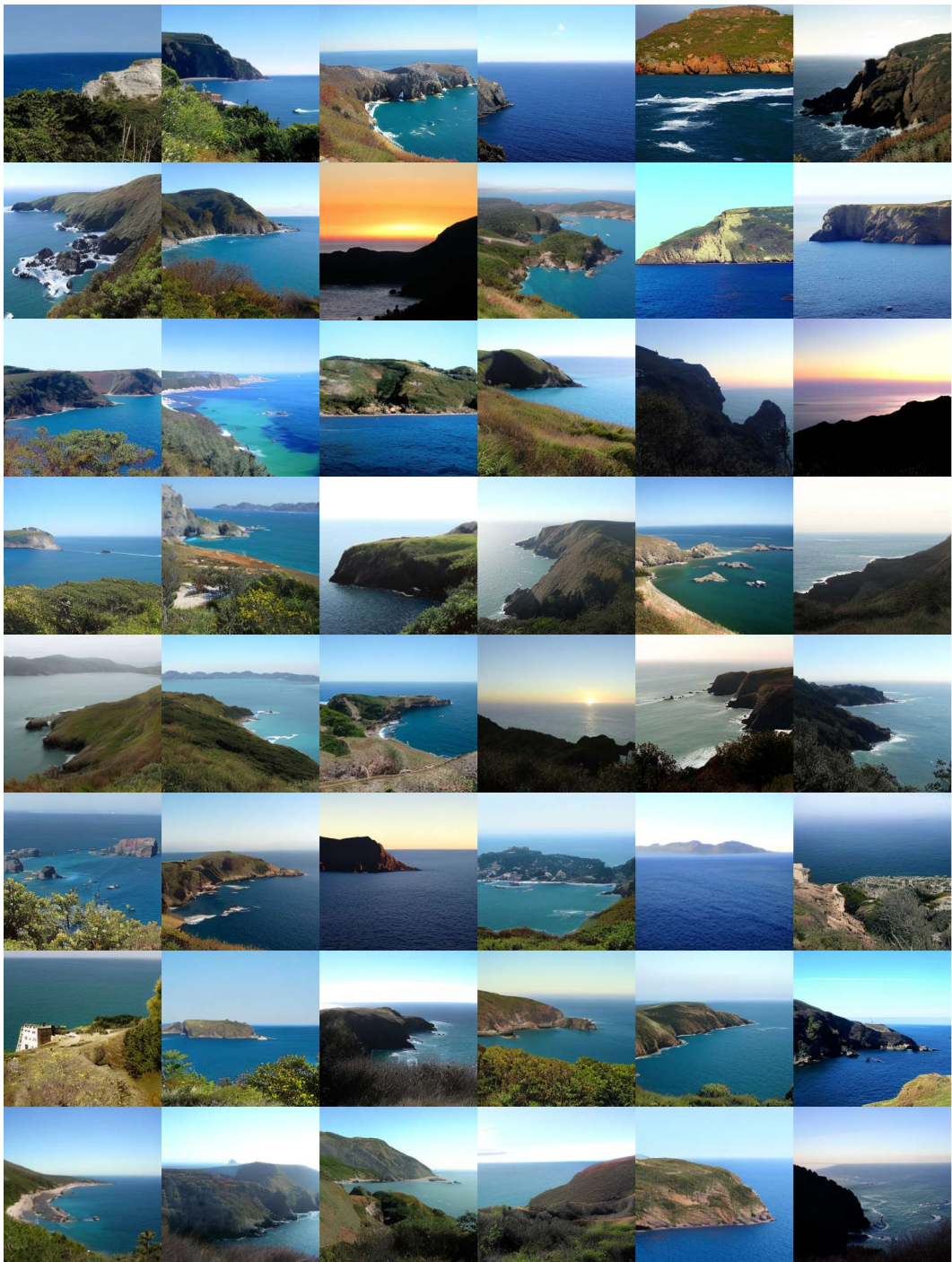


Figure 18: 256×256 samples of *ComboStoc-XL/2 800K*. Classifier-free guidance scale = 4.0. Class label = “promontory, headland, head, foreland” (976).

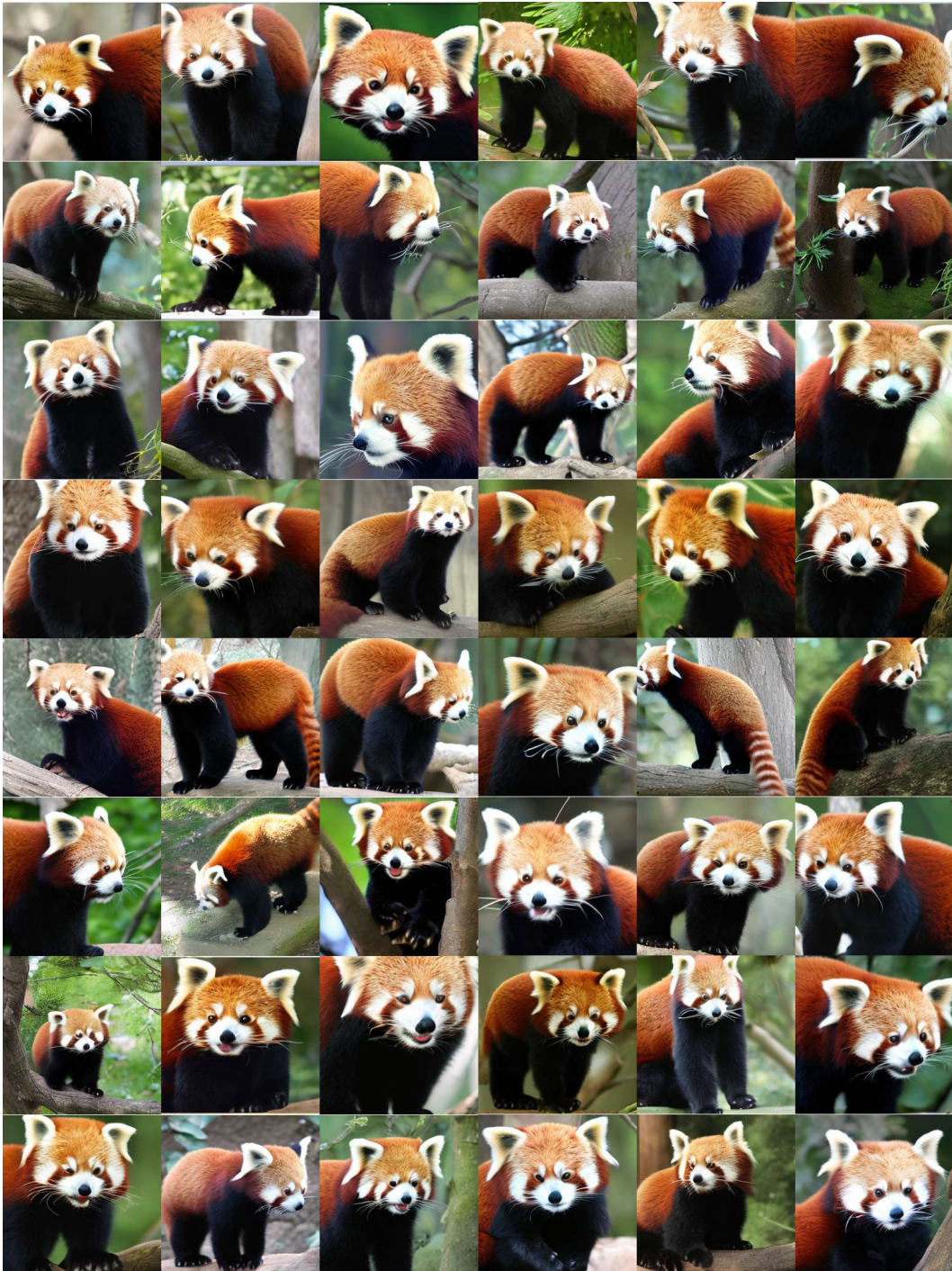


Figure 19: 256×256 samples of *ComboStoc-XL/2* 800K. Classifier-free guidance scale = 4.0. Class label = “lesser panda, red panda, panda, bear cat, cat bear, *Ailurus fulgens*” (387).



Figure 20: 256×256 samples of *ComboStoc-XL/2* 800K. Classifier-free guidance scale = 4.0. Class label = “geyser” (974).



Figure 21: 256×256 samples of *ComboStoc-XL/2 800K*. Classifier-free guidance scale = 4.0. Class label = “giant panda, panda, panda bear, coon bear, *Ailuropoda melanoleuca*” (388).



Figure 22: 256×256 samples of *ComboStoc-XL/2* 800K. Classifier-free guidance scale = 4.0. Class label = “alp” (970).



Figure 23: 256×256 samples of *ComboStoc-XL/2 800K*. Classifier-free guidance scale = 4.0. Class label = “Arctic fox, white fox, *Alopex lagopus*” (279).



Figure 24: 256×256 samples of *ComboStoc-XL/2* 800K. Classifier-free guidance scale = 4.0. Class label = “volcano” (980).

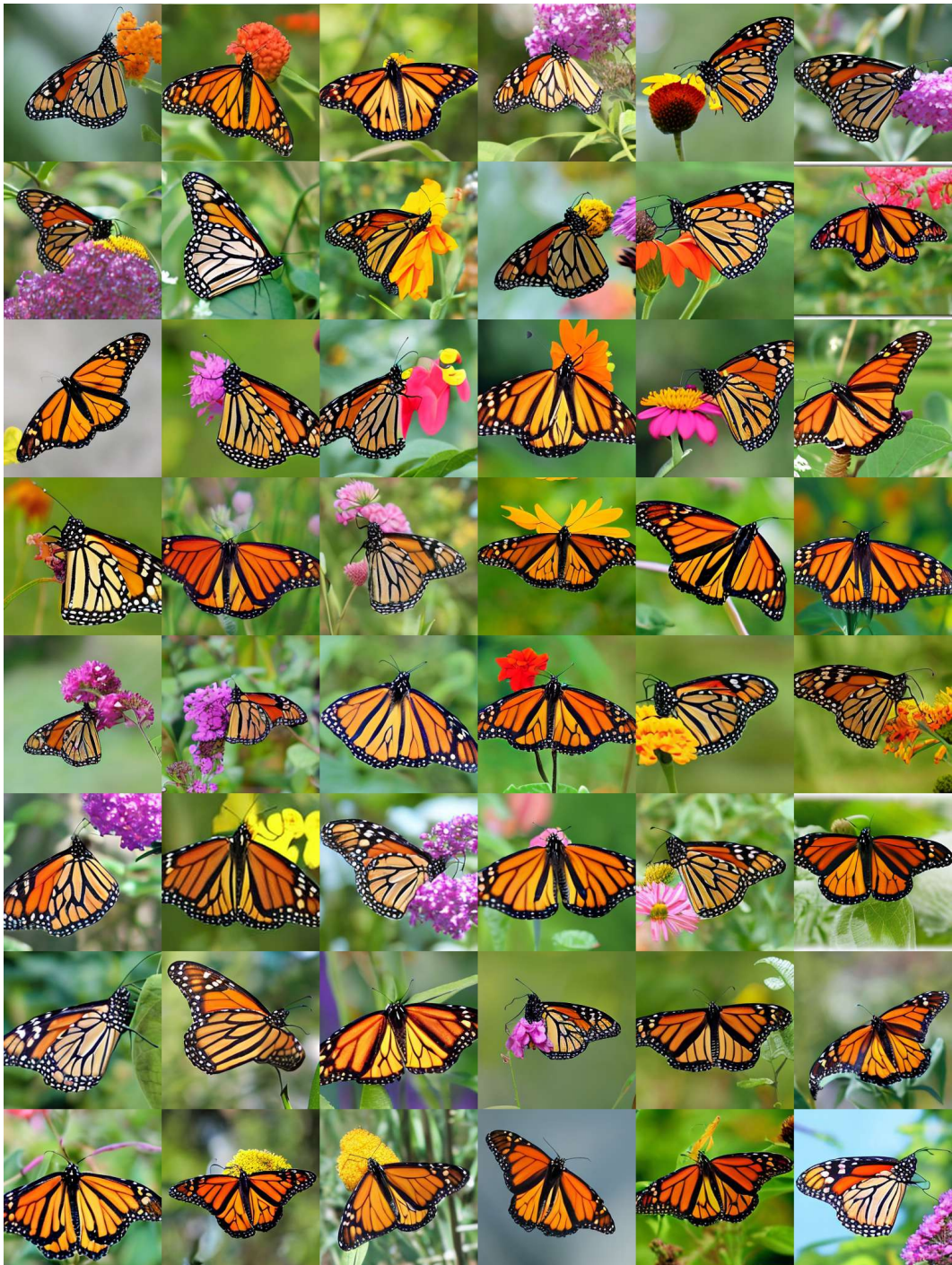


Figure 25: 256×256 samples of *ComboStoc-XL/2* 800K. Classifier-free guidance scale = 4.0. Class label = “monarch, monarch butterfly, milkweed butterfly, *Danaus plexippus*” (323).



Figure 26: 256×256 samples of *ComboStoc-XL/2* 800K. Classifier-free guidance scale = 4.0. Class label = “valley, vale” (979).



Figure 27: 256×256 samples of *ComboStoc-XL/2* 800K. Classifier-free guidance scale = 4.0. Class label = “macaw” (88).



Figure 28: 256×256 samples of *ComboStoc-XL/2 800K*. Classifier-free guidance scale = 4.0. Class label = "snail" (113).



Figure 29: 256×256 samples of *ComboStoc-XL/2* 800K. Classifier-free guidance scale = 4.0. Class label = “Eskimo dog, husky” (248).

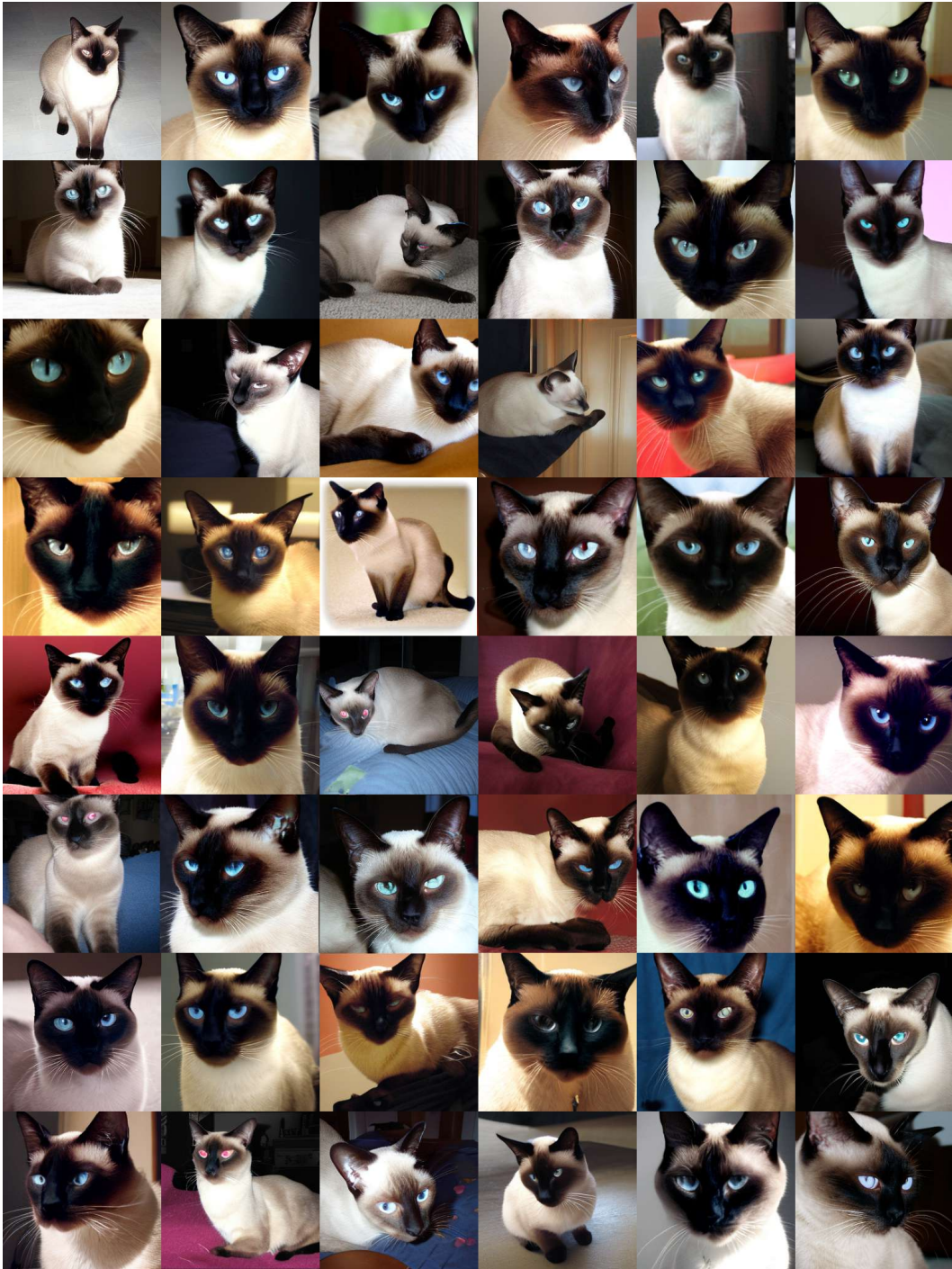


Figure 30: 256×256 samples of *ComboStoc-XL/2* 800K. Classifier-free guidance scale = 4.0. Class label = “Siamese cat, Siamese” (284).